Article

Structure and Electrochemical Properties of Bronze Phase Materials Containing Two Transition Metals

Yunkai Luo, Etienne Le Calvez, Yucheng Zhou, Éric Gautron, Éric Quarez, Molleigh Preefer, Olivier Crosnier, Johanna Nelson Weker, Laurent Pilon, Thierry Brousse, and Bruce Dunn*

Read Online

ACCESS | Metrics & More | Article Recommendations | Supporting Information

ABSTRACT: Bronze phase transition-metal oxides have recently attracted attention as high-rate lithium-ion battery anode materials. Their crystal structures are distinguished by large tunnels and an open framework, facilitating lithium-ion diffusion and high-rate charge−discharge properties. The presence of two transition metals also offers a route to achieve high energy density from multielectron redox. In this paper, we report the chemistry, structure, and electrochemical properties of two different bronze phase compositions having the same stoichiometry: $W_3Nb_2O_{14}$ and $Mo_3Nb_2O_{14}$. These materials provide insight into how the transition metals affect the electrochemical behavior and structural stability of bronze phase materials. $Mo_3Nb_2O_{14}$ exhibits greater than 1 electron redox per transition metal leading to lithium capacities above 200 mAh g^{-1} at C/2 but is unable to maintain this high capacity at high rates due to incomplete Mo redox reactions. In contrast, $W_3Nb_2O_{14}$ exhibits reversible redox reactions and retains its open structure on cycling. This study highlights the potential of bronze phase materials containing two transition metals to exhibit fast charging properties with a high energy density.
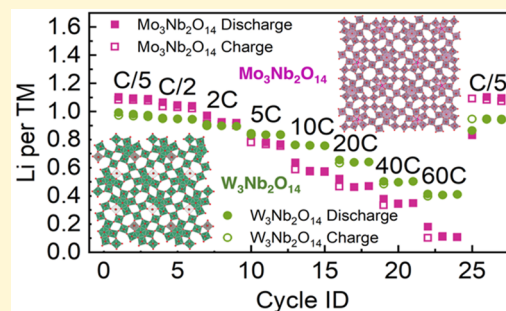
1. INTRODUCTION

Any significant effort at achieving net-zero emissions in the next few decades will involve electrification of transportation, which accounted for 66% of total U.S. petroleum consumption in 2020.[1] Lithium-ion batteries (LIBs) play a prominent role in realizing electric vehicle (EV) technology, and improved performance will be necessary to overcome limitations in driving range and charging time.[2] For this reason, there is great interest in developing energy-storage materials that can rapidly undergo charge−discharge reactions without compromising a high energy density.

Although graphite is the commercial material of choice for the negative electrode material in lithium-ion batteries, it is susceptible to lithium dendrite formation when operated at high charge rates, especially at low potentials.[3] This is one reason why another lithium intercalation material, $Li_4Ti_5O_{12}$, has been widely utilized as a high-rate negative electrode despite its higher operating potential (1.55 V vs Li/Li$^+$) and lower capacity of lithium (175 mAh g^{-1}).[4] Over the past several years, a number of other intercalation material systems have emerged that offer the promise of high energy densities and operation at lower potentials. In particular, Wadsley-Roth crystallographic shear phases are attractive as systems such as $TiNb_2O_7$,[5] PNb_9O_{25},[6] $W_5Nb_{16}O_{55}$,[7] and others have generated considerable interest with their high theoretical capacity, rapid ion conduction, and ability to accommodate greater than 1 Li per transition metal. The multielectron redox for Nb, which

arises from its multiple valence states,[6] also exists with other transition metals, including V,[8,9] Mo,[10−12] and W,[13,14] and broadens the scope of fast-charging electrochemical energy storage materials.

Bronze phases tend to possess a more open framework than Wadsley-Roth structures and represent a promising choice for fast-charging electrode materials. First discovered in 1824,[15,16] the most common bronze family is the tungsten bronzes, which are well-known nonstoichiometric compounds with the general formula M_xWO_3 (M = alkali metals). Depending on the amount and size of the alkali metal, tetragonal tungsten bronzes or hexagonal tungsten bronzes can be formed.[17] The hexagonal channels in the M_xWO_3 bronze framework ensure rapid ion diffusion,[18] and the presence of edge-sharing octahedra in the *a-b* plane of the bronze phase structure effectively reduces the band gap energy,[19] which is beneficial for lithium-ion battery electrodes.[20] However, the unfavorable occupation of electrochemically inactive alkali metal ions reduces the number of insertion sites. In contrast, reduced tungsten oxides, such as $W_{18}O_{49}$,[14,21] could have more than 1.2
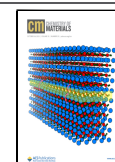
lithium uptake per tungsten and still retain the tunnel-like feature of the bronze structure by replacing the alkali metal with W^{5+}. The substitution of reduced transition metals with alkali ions provides more lithium insertion sites in the structure.

Recently, the tetragonal tungsten−niobium bronze phase[22−24] has received attention as an anode offering high power and energy for LIBs. Griffith et al. reported that the $Nb_{18}W_{16}O_{93}$ bronze phase has redox reaction contributions from both tungsten and niobium and exhibited greater than 1 electron redox at rates below 1C and a capacity over 100 mAh g^{-1} at rates as high as 60C.[7] Yao et al. observed that the $W_{10.3}Nb_{6.7}O_{47}$ bronze phase could maintain 80% capacity retention as the rate increased from 0.5C (135 mAh g^{-1}) to 20C (108 mAh g^{-1}).[25] By variation of the transition metals, the potential range changes accordingly. Kaveevivitchai et al. reported that $Mo_{2.48}VO_{9.93}$ bronze could function as a positive electrode material for LIBs as it delivers over 300 mAh g^{-1} by accommodating 6 lithium per unit formula between 3.9 and 1.5 V (vs Li/Li$^+$).[26] There is also evidence that the second transition metal could provide stability for the open bronze structure.[27,28] For example, the reduced molybdenum oxide, Mo_5O_{14},[29] which possesses a similar bronze phase tunnel-like structure, is able to achieve multielectron redox. Although Mo_5O_{14} is a metastable phase and only stabilizes in a narrow temperature range, a thermodynamically stable phase, $Mo_3Nb_2O_{14}$, could be obtained by substituting Mo^{5+} with Nb^{5+} without changing the tunnel-like bronze structure.[30] Fang et al. reported that the $Mo_3Nb_2O_{14}$ bronze phase can operate as a high-rate anode material for lithium-ion batteries, delivering 75 mAh g^{-1} at a 5C rate.[31] While these examples show promising electrochemical results, there is the prospect that a better understanding of the role of the two transition metals, their redox reactions, and structural changes on charge and discharge can lead to the development of bronze phase materials as high-performance battery electrode materials.

In this study, we compare the structures and electrochemical properties and determine the role of the transition metal in two bronze phase materials with the same stoichiometry: $Mo_3Nb_2O_{14}$ and $W_3Nb_2O_{14}$. $Mo_3Nb_2O_{14}$, which has a more open structure than $W_3Nb_2O_{14}$, exhibits greater than 1 electron redox per transition metal at rates up to C/2 as it benefits from Mo redox reactions. However, the material is unable to maintain this high capacity at high rates due to the irreversibility of the Mo redox. By comparison, $W_3Nb_2O_{14}$ achieves 1 electron per transition metal at rates up to nearly 1C and exhibits much better rate performance than $Mo_3Nb_2O_{14}$ despite having a more compact structure. The combination of *in situ* X-ray diffraction (XRD), *operando* XRD, *ex situ* X-ray photoelectron spectroscopy (XPS), and entropic potential measurements enables us to characterize and understand the structural and chemical features associated with the transition-metal redox reactions which determine the electrochemical results. The results provide insight into the design of bronze phase materials for fast-charging electrochemical energy storage materials.

2. EXPERIMENTAL METHODS

Solid-State Synthesis of $W_3Nb_2O_{14}$ and $Mo_3Nb_2O_{14}$. Although the two bronzes possess the same stoichiometry, the temperatures used in their solid-state synthesis are very different, because of the precursor oxides. The $W_3Nb_2O_{14}$ samples were obtained by mixing WO_3 (Alfa, Morton Thiokol Inc., 99.7%) and Nb_2O_5 (Sigma-Aldrich,

99.99% trace metal basis) powder with the correct stoichiometry with an agate mortar and pestle for 10 min. The well-mixed powder was placed in an alumina crucible and transferred into a programmed box furnace at 1050 °C for 12 h with a 5 °C min^{-1} heating rate. When the $W_3Nb_2O_{14}$ powder was cooled to room temperature, the color of $W_3Nb_2O_{14}$ shifted from white to gray. The $Mo_3Nb_2O_{14}$ powder was prepared similarly by mixing MoO_3 (Sigma-Aldrich, 99.97% trace metal basis) and Nb_2O_5 (Sigma-Aldrich, 99.99% trace metal basis) powder in the correct stoichiometry. Since the melting temperature of MoO_3 is 795 °C, the synthesis temperature for $Mo_3Nb_2O_{14}$ is significantly lower. For this material, the mixed powder was heated to 750 °C for 12 h with a 5 °C min^{-1} heating rate and cooled to room temperature.

Powder X-ray Diffraction. X-ray diffraction (XRD) was carried out using a PANalytical X'Pert Pro diffractometer (Malvern Panalytical, Almelo, Netherlands). An X'Celerator detector with Cu $K_{\alpha 1}$-$K_{\alpha 2}$ (λ = 1.54060, 1.54439 Å) radiation was used. The acceleration voltage and current were 40 kV and 40 mA, respectively. With a step scan of 0.0167°, diffraction patterns were collected between 20° and 90° (2θ). Le Bail refinements were performed by using a pseudo-Voigt function for the peak profile.[32]

Scanning Electron Microscopy/Energy-Dispersive X-ray. Scanning electron microscopy (SEM; FEI Nova NanoSEM230) images were obtained by using 10 keV accelerating voltage with a 5 mm working distance. A thin layer of gold was sputtered for 1 min on the surface of the samples to alleviate the charging effect and produce better quality images. The energy-dispersive X-ray (EDX) elemental map was collected at different focused regions for 5 min each.

Scanning/Transmission Electron Microscopy. Scanning/transmission electron microscopy (S/TEM) was used to characterize the structural features of the phases. Powders were dispersed in ethanol and then deposited on a holey carbon-coated copper grid before insertion in a probe-corrected S/TEM Themis Z G3 (Thermo Fisher Scientific). High-angle annular dark-field (HAADF-STEM) images were acquired at 80 kV, with 20 mrad convergence angles and 52−200 mrad collection angles. To limit sample degradation, the Drift Corrected Frame Integration (DCFI) mode with 20 frames (0.8 s per frame) was used to obtain high-resolution HAADF-STEM images. Energy-dispersive X-ray spectroscopy (EDS) was performed with the 4-SDD detector Super-X system.

Electrochemical Characterization. The as-prepared $M_3Nb_2O_{14}$ (M = W, Mo) sample was mixed with carbon black (TIMCAL Super P) and poly(vinylidene fluoride) (PVDF) with a mass ratio of 75% active material, 15% carbon black, and 10% PVDF binder. The appropriate amount of 1-methyl-2-pyrrolidinone (NMP) was added, and after mixing for 10 min with mortar and pestle, the slurry was cast onto a carbon-coated Al foil using a doctor blade. The uniform cast slurry was placed on a 40 °C hot plate to dry overnight in the fume hood and continued drying at 110 °C in a vacuum oven for 5 h. The average mass loading for each cell was 2 mg cm^{-2}. The 2032 type coin cells were assembled in an argon-filled glovebox (H_2O < 0.1 ppm, O_2 < 0.1 ppm). Whatman GF/C glass microfiber filters served as separators, and the electrolyte was 1 M LiPF$_6$ in 1:1 volume ratio of ethylene carbonate (EC)/dimethyl carbonate (DMC), and polished lithium foil functioned as the counter and reference electrodes. A BioLogic VMP-300 Potentiostat was used for galvanostatic (GV) cycling, cyclic voltammetry (CV), and galvanostatic intermittent titration technique (GITT) measurements. The theoretical capacity was calculated based on 1 electron redox per transition metal per unit formula. The theoretical capacities of $Mo_3Nb_2O_{14}$ and $W_3Nb_2O_{14}$ are 192.1 and 139.4 mAh g^{-1}, respectively. Thus, 1C corresponds to specific currents of 192.1 and 139.4 mA g^{-1} for $Mo_3Nb_2O_{14}$ and $W_3Nb_2O_{14}$, respectively. Based on a previous study on $Mo_3Nb_2O_{14}$[31] and the results of potential window opening experiments shown in [Figure S1](#), the 1.5−3.0 V (vs Li/Li$^+$) potential range was chosen for both cyclic voltammetry (CV) and galvanostatic (GV) charge−discharge measurements for $Mo_3Nb_2O_{14}$. Similarly, the appropriate potential range for $W_3Nb_2O_{14}$ was chosen by performing voltammetric potential window opening experiments as shown in [Figure S1](#). The results reveal that cycling below 1.2 V irreversibly increases the
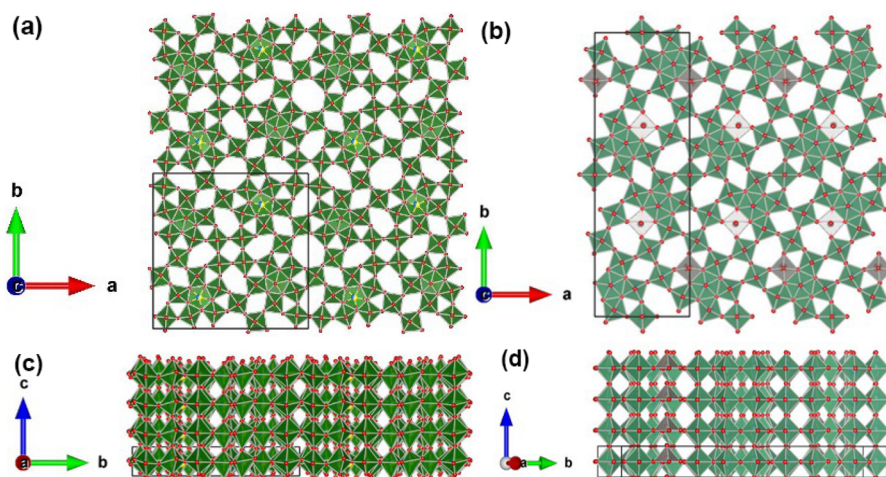
Figure 1. Unit cell of (a) $Mo_3Nb_2O_{14}$ or (b) $W_3Nb_2O_{14}$ projected down the c axis; the $W_3Nb_2O_{14}$ structure is depicted based on the CIF file of $W_{10.7}Nb_{6.3}O_{47}$. The unit cell of (c) $Mo_3Nb_2O_{14}$ or (d) $W_3Nb_2O_{14}$ projected down the a direction. The bipyramidal pentagonal and octahedral sites in $Mo_3Nb_2O_{14}$ are randomly occupied by Mo and Nb. The $W_3Nb_2O_{14}$ possesses the same tunnel structure as $W_{10.7}Nb_{6.3}O_{47}$ but with a different occupancy of transition metal, which is described in Figure S4. The crystal structures were depicted using VESTA.

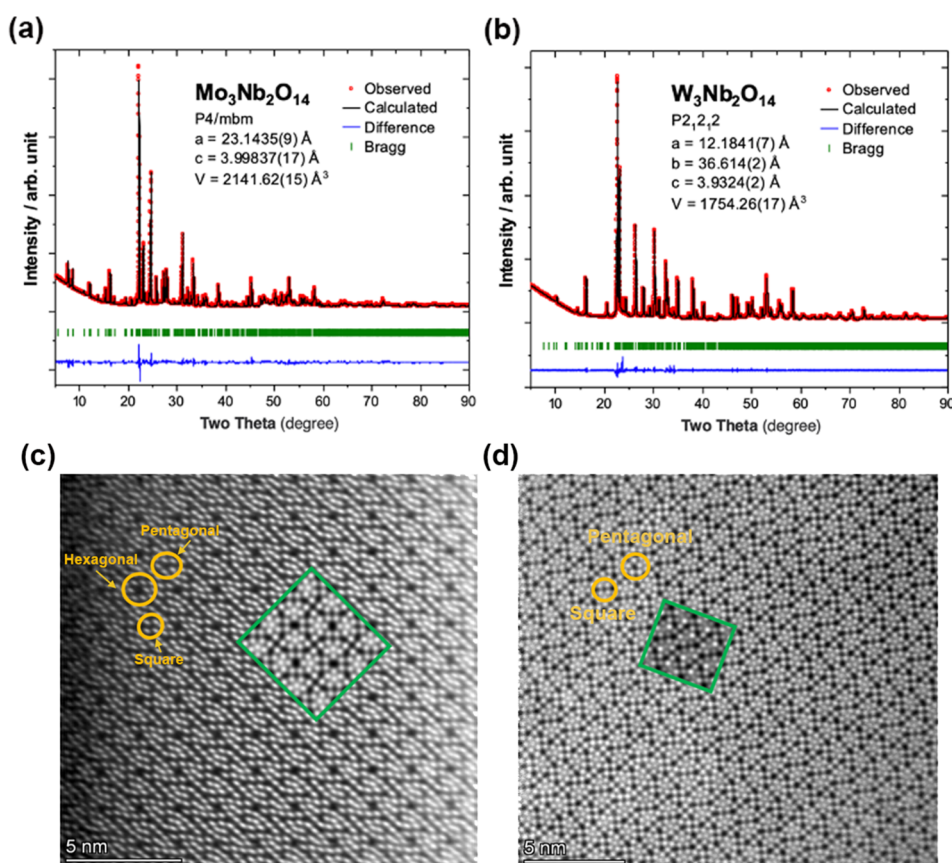**Figure 2.** XRD refinement result of (a) $Mo_3Nb_2O_{14}$ and (b) $W_3Nb_2O_{14}$. HAADF-STEM images of (c) $Mo_3Nb_2O_{14}$ and (d) $W_3Nb_2O_{14}$; the scale bar is 5 nm. The green rectangle inside the images depicts the HAADF simulated images of 2×2 unit cell of $Mo_3Nb_2O_{14}$ and 3×1 unit cell of $W_3Nb_2O_{14}$ in the a-b plane.

anodic current, which indicates the possibility of conversion reactions or decomposition. Thus, 1.2−3.0 V (vs Li/Li$^+$) was selected as the appropriate cycling potential window for evaluating $W_3Nb_2O_{14}$.

X-ray Photoelectron Spectroscopy (XPS). The XPS electrodes were cycled by using Swagelok-type cells. The recovered *ex situ* electrodes were washed in pure EC/DMC solvent with 1:1 volume ratio at least three times to remove residual electrolyte in the electrode and then soaked in NMP solvent for 1 day to remove all

PVDF binder in the electrode for high-quality XPS signals. The electrode was then heated at 120 °C for 5 h to evaporate the residual NMP in the argon-filled glovebox and dried under a vacuum overnight before testing. To avoid possible oxidation from occurring, the samples were loaded in an air-free transfer carrier in an argon-filled glovebox. The survey spectrum and detailed Mo, Nb, and W scans were collected by XPS (Kratos Axis Ultra) with a monochromatic aluminum X-ray source by using a voltage of 15 kV

and emission current of 10 mA. A pass energy of 20 eV and a dwell time of 800 ms for each element with an average of 20 scans were used for the detailed scans.

The CasaXPS software was used to fit the collected data and reveal the oxidation states of the transition metals. All spectra were referenced to C 1s peak of 248.8 eV. The fitting of d-orbitals of Mo and Nb and f-orbitals of W were area-constrained to $d_{5/2}/d_{3/2} = 3:2$ and $f_{7/2}/f_{5/2} = 4:3$ area ratio, respectively. The same full width at half-maximum (fwhm) and Lorentzian asymmetric line shape conditions were fixed in the fitting. Shirley-type background was applied to all fittings, and the peak splitting energy of 2.17, 2.78, and 3.15 eV was applied to W_{4f}, Nb_{3d}, and Mo_{3d}, respectively.

In Situ XRD and Operando XRD. *In situ* XRD patterns were collected using a homemade Leriche-like cell.[33] In the charge−discharge experiment, a current of 20 mA g$^{−1}$ was applied for 60 min and relaxed for 30 min for XRD pattern acquisition. Le Bail analysis of the XRD data were performed using JANA2006.

Operando X-ray diffraction was collected on beamline 11−3 (12.7 keV) at the Stanford Synchrotron Radiation Lightsource (SSRL) in transmission geometry using pouch cells. The pouch cells were assembled in an Ar-filled glovebox (O$_2$ < 0.1 ppm, H$_2$O < 0.1 ppm) with the fabricated electrodes described above, a Celgard 2500 separator soaked in LP40 electrolyte, and a Li metal counter electrode, vacuum sealed in an aluminized pouch. The pouches were encased in pressure plates fabricated from poly(lactic acid) applied with 4 screws at each corner. The screws were tightened with a torque screwdriver set to 8 in-oz. The cells were mounted onto the beamline and concurrently cycled at a constant current of C/3 (64 mA g$^{−1}$ for Mo$_3$Nb$_2$O$_{14}$ and 46.5 mA g$^{−1}$ for W$_3$Nb$_2$O$_{14}$). The voltage limits for Mo$_3$Nb$_2$O$_{14}$ were 1.5 and 3.0 V, and the voltage limits for W$_3$Nb$_2$O$_{14}$ were 1.2 and 3.0 V, both beginning with discharge. Images were collected with 10 s exposures on a Rayonix MX225 CCD area detector with a sample-to-detector distance of 150 mm. Each cell was measured approximately every 4 min. The data were calibrated using LaB6 and reduced to one-dimensional (1D) patterns using GSAS II.

Potentiometric Entropy Measurements. The open-circuit voltage U_{OCV} (C_m,T) and entropic potential ∂U_{OCV} $(C_m,T)/\partial T$ of coin cells were measured as functions of specific capacity C_m using the technique and setup described in refs 34−36. Measurements were performed on coin cells with Mo$_3$Nb$_2$O$_{14}$ or W$_3$Nb$_2$O$_{14}$ working electrodes and lithium metal counter electrodes. During the measurements at 20 °C, a series of constant current pulses at C/10 spanning 30 min were imposed, each followed by a relaxation period of 270 min. Within the relaxation periods, a steplike temperature profile was applied to the coin cell from 15 to 25 °C in 5 °C increments with a thermoelectric cold plate (TE technology, CP-121) while the corresponding coin cell potential evolution was recorded with a potentiostat (BioLogic, VSP-300). Toward the end of every temperature step, we verified that the coin cell had reached thermodynamic equilibrium based on two criteria: (i) the temperature difference between the cold plate and the top of the coin cell was less than 0.1 °C, and (ii) the time rate of change of the open-circuit voltage ∂U_{OCV} $(C_m,T)/\partial$t was less than 1 mV h$^{−1}$.

3. RESULTS AND DISCUSSION

Characterization of Bronze Structures. Phase pure Mo$_3$Nb$_2$O$_{14}$ and W$_3$Nb$_2$O$_{14}$ were synthesized by the solid-state method mentioned above. The unit cell structures of Mo$_3$Nb$_2$O$_{14}$ and W$_3$Nb$_2$O$_{14}$ are depicted in Figure 1(a,c) and Figure 1(b,d), respectively. Although the two bronzes have the same stoichiometries, they possess different unit cells and space groups. Laboratory XRD and the Le Bail XRD refinement results for Mo$_3$Nb$_2$O$_{14}$ and W$_3$Nb$_2$O$_{14}$ are shown in Figure 2a and Figure 2b, respectively. The refined lattice parameters of Mo$_3$Nb$_2$O$_{14}$ are $a = b = 23.1435$ (9) Å, $c = 3.99837$ (17) Å, and $V = 2141.62$ (15) Å^3, which agrees well with a previous report.[31] The tungsten−niobium bronze phase material W$_3$Nb$_2$O$_{14}$ was first identified by Bouillaud et al. in

1968,[37] and the structure of W$_3$Nb$_2$O$_{14}$ is analogous to W$_{10.7}$Nb$_{6.3}$O$_{47}$. Thus, the parameters of the W$_{10.7}$Nb$_{6.3}$O$_{47}$ phase were used for W$_3$Nb$_2$O$_{14}$ refinement. The refinement results show that the cell parameters are $a = 12.1841$ (7) Å, $b = 36.614$ (2) Å, $c = 3.9324$ (2) Å, and $V = 1754.26$ (17) Å^3, which are all smaller than the W$_{10.7}$Nb$_{6.3}$O$_{47}$ phase. This might be due to the larger ionic radius of Nb^{5+} compared with W^{6+}.

The SEM images shown in Figures S2 and S3 indicate that the average particle sizes of as-prepared samples are similar, around 1−5 μm. The shape of the particles for both compositions is rod-like, which is commonly observed in bronze materials due to preferential growth in the c direction.[38] The EDX elemental map shown in Figures S2 and S3 indicates the uniform distribution of all transition metals. The statistical calculation from the EDX elemental map is shown in Table S1 for both materials. The W or Mo to Nb ratio is very close to 1.5, which implies an accurate stoichiometry and almost no loss of precursors during synthesis.

High-resolution STEM carried out in the current study [Figures 2(c,d)] provides greater details of the structural features than those reported previously for both bronze phase materials.[25,39] The HAADF-STEM image acquired on Mo$_3$Nb$_2$O$_{14}$ (Figure 2c) along the c axis matches perfectly with the superimposed 2 × 2 unit cell pattern in the green rectangular region that was simulated with Dr Probe software[40] using the structure described in Figure 1a. The characteristic hexagonal, pentagonal, and quadrilateral channels are depicted by yellow circles. The HAADF-STEM image of W$_3$Nb$_2$O$_{14}$ is composed mainly of pentagonal and quadrilateral channels highlighted by yellow circles (Figure 2d). The 3 × 1 unit cell simulated pattern is outlined by the green rectangular area. The EDX elemental maps in Figure S4 show the preferential cation ordering in a W$_3$Nb$_2$O$_{14}$ unit cell. The Nb atoms occupy the center of the pentagonal bipyramid site, while the edge-sharing octahedra with pentagonal bipyramids are randomly occupied by W and Nb. The pentagonal channels are linked by one octahedron preferentially occupied by W. The occupancy of W and Nb in W$_3$Nb$_2$O$_{14}$ is different from the W$_{10.7}$Nb$_{6.3}$O$_{47}$ phase; this variation may be due to the slight difference in composition. Although most regions of W$_3$Nb$_2$O$_{14}$ in the TEM images exhibit the proposed W$_{10.7}$Nb$_{6.3}$O$_{47}$-type structure, there are some regions indicating the existence of defects, as shown in Figure S5. This might be associated with the intergrowth of ReO$_3$-type niobium and tungsten octahedra that were commonly observed in the niobium tungsten oxide system.[41,42] Since the amount of intergrowth is relatively negligible, the fundamental electrochemical responses of W$_3$Nb$_2$O$_{14}$ are assumed to be mostly related to the main bronze phase structure.

Electrochemical Characterization. Galvanostatic charge−discharge experiments were carried out at various rates for both bronze phase materials [Figure 3(a−c)]. The capacity of Mo$_3$Nb$_2$O$_{14}$ at rates between C/10 and C/2 is greater than the theoretical capacity of 192 mAh g$^{−1}$ which is based on a total of 5 electron redox per unit formula (i.e., 1 electron per transition-metal ion). Thus, one of the transition-metal ions provides more than 1 electron redox at these rates. The capacity of W$_3$Nb$_2$O$_{14}$, discharged to a lower potential (1.2 vs 1.5 V), reaches its theoretical capacity of 139.4 mAh g$^{−1}$ only at the rate of C/10, which is much smaller than that of Mo$_3$Nb$_2$O$_{14}$ at the same C-rate (Figure 3a). Moreover, the lithium per transition metal analysis (Figure 3b) shows that more electron transfer occurs in W$_3$Nb$_2$O$_{14}$ than in
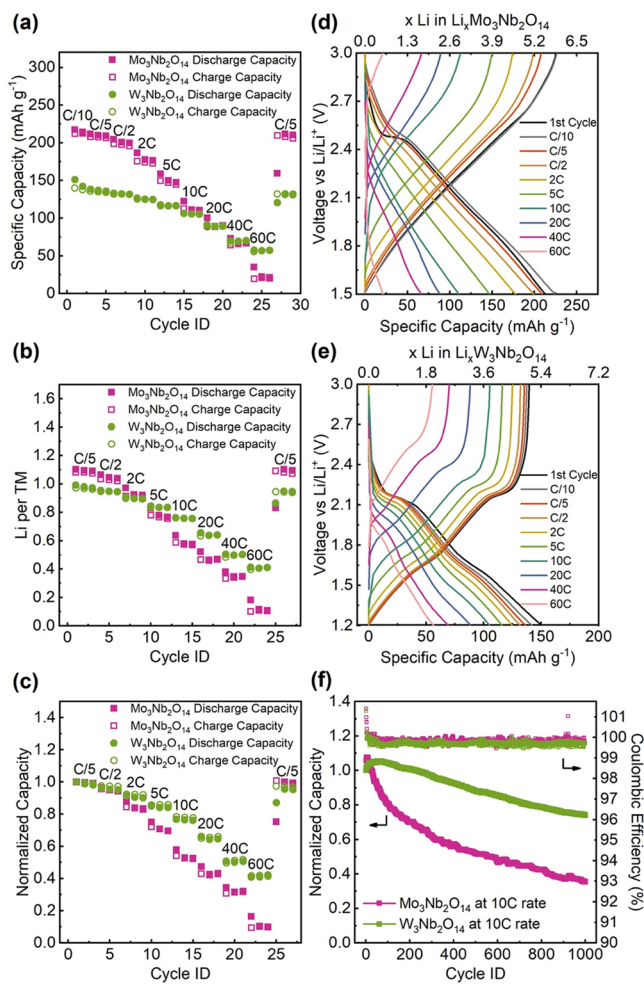
Figure 3. (a−c) Comparison of variable-rate galvanostatic cycling in terms of specific capacity, lithium per transition metal, and normalized capacity at C/5 between $Mo_3Nb_2O_{14}$ and $W_3Nb_2O_{14}$; the galvanostatic curve of voltage as a function of specific capacity for (d) $Mo_3Nb_2O_{14}$ and (e) $W_3Nb_2O_{14}$. (f) Comparison of long-term galvanostatic cycling at 10C for 1000 cycles for $Mo_3Nb_2O_{14}$ and $W_3Nb_2O_{14}$. The specific capacity values for the first cycle at 10C for each material represent the reference values for the normalized capacity.

$Mo_3Nb_2O_{14}$ when the rate is higher than 2C. Using the specific capacity at C/5 as the reference value, normalized capacities were determined for both bronze phases (Figure 3c). Above 5C the normalized capacity for $W_3Nb_2O_{14}$ was significantly greater than that for $Mo_3Nb_2O_{14}$.

The galvanostatic curve of $Mo_3Nb_2O_{14}$ (Figure 3d) shows a clear plateau region only for the first cycle. Thereafter, the plateau becomes less apparent and even disappears after 2 cycles at a C/10 rate, suggesting that irreversible reactions might occur in $Mo_3Nb_2O_{14}$. The almost linear voltage profile over the entire potential window is a signature of a pseudocapacitive response.[43] In $W_3Nb_2O_{14}$, there are two changes in slope at 2.1 and 1.7 V (Figure 3e) which may be attributed to two different solid solution regions.[24]

The long-term cycling performance for both materials was evaluated over 1000 cycles at 10C (Figure 3f). Using the first cycle specific capacity at 10C as the reference value for the normalized capacity, the capacity retention of $W_3Nb_2O_{14}$ is more than two times higher than that of $Mo_3Nb_2O_{14}$. A

separate set of galvanostatic cycling experiments indicates that the capacity fade with $Mo_3Nb_2O_{14}$ is not due to prior cycling (Table S2). Overall, the various GV experiments indicate that although $Mo_3Nb_2O_{14}$ delivers higher capacity at low rates and exceeds 1 electron per transition-metal ion, the capacity retention and cycling performance of $W_3Nb_2O_{14}$ is much better. This leads to an interesting insight that the $W_3Nb_2O_{14}$ with its relatively compact structure performs better than the more open structured $Mo_3Nb_2O_{14}$ in terms of electrode kinetics and capacity at high rates.

Electrode Kinetics. Both materials were investigated using cyclic voltammetry (CV) at a 0.1 mV s^{-1} scan rate. For the first 4 cycles [Figures 4(a,b)], both materials exhibit a box-like CV
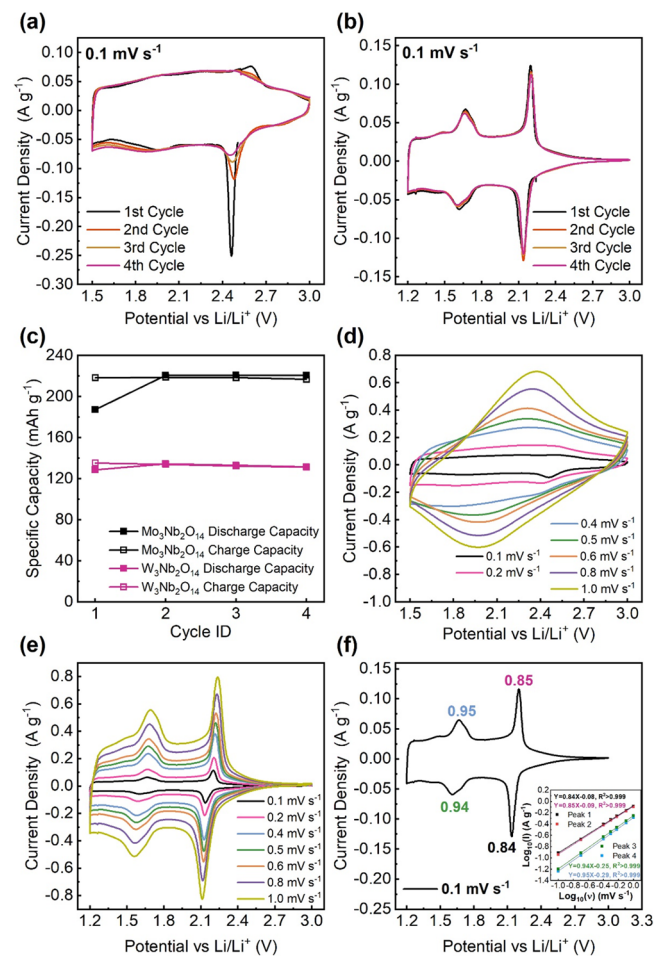

Figure 4. CV of (a) $Mo_3Nb_2O_{14}$ and (b) $W_3Nb_2O_{14}$ at a scan rate of 0.1 mV s^{-1} for the first 4 cycles. (c) The comparison of calculated discharged and charged specific capacity from CV at a scan rate of 0.1 mV s^{-1} for the first 4 cycles between $Mo_3Nb_2O_{14}$ and $W_3Nb_2O_{14}$; the CV curves of (d) $Mo_3Nb_2O_{14}$ and (e) $W_3Nb_2O_{14}$ at sweep rates varying from 0.1 to 1 mV s^{-1}. (f) Calculated b-values of two cathodic and anodic redox peaks of $W_3Nb_2O_{14}$; the detailed b-value fittings of peaks are shown in the inset image.

curve, which is representative of a capacitive-type response. There are, however, some key differences. With $W_3Nb_2O_{14}$, two reversible peaks are superimposed on the rectangular box with one broad peak and one sharp peak at 1.7 and 2.1 V (vs Li/Li$^+$), respectively. For $Mo_3Nb_2O_{14}$, the CV curve also exhibits a capacitive shape but with one irreversible sharp peak at 2.4 V (vs Li/Li$^+$), the intensity of which keeps decreasing
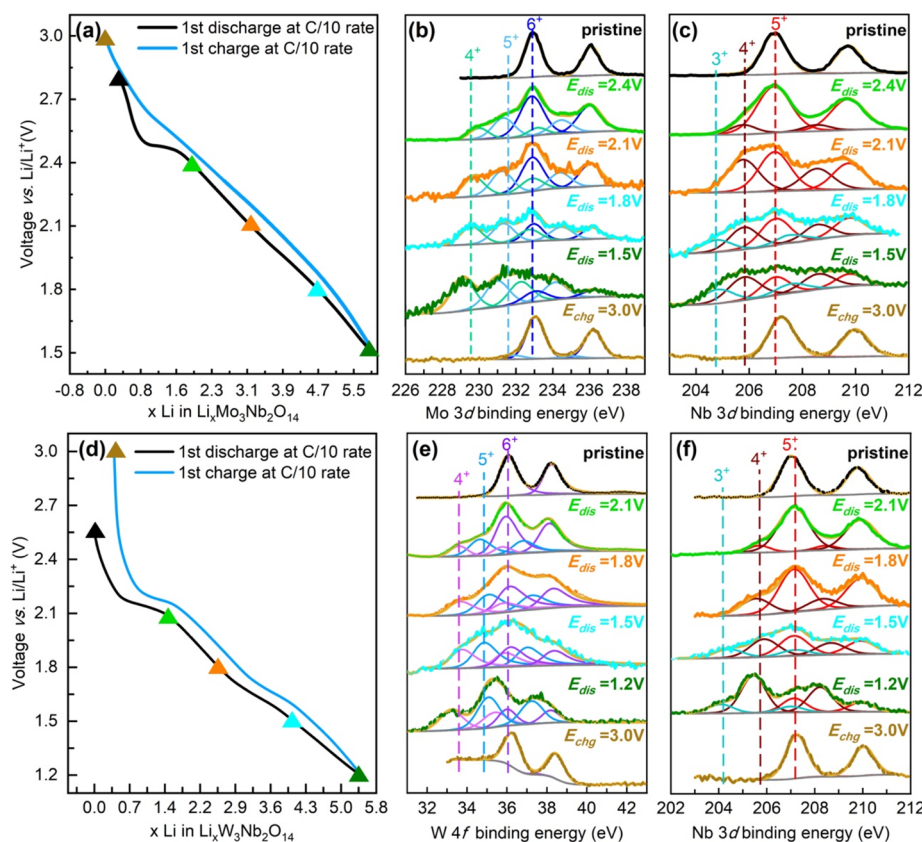
Figure 5. (a) The first galvanostatic discharge and charge for Li insertion in $Mo_3Nb_2O_{14}$ and the potentials corresponding to the XPS spectra in the Mo 3d binding energy region (b) and Nb 3d binding energy region (c). Similarly, (d) is the first galvanostatic discharge and charge for Li insertion in $W_3Nb_2O_{14}$ and the potentials corresponding to XPS spectra in the W 4f binding energy region (e) and the Nb 3d binding energy region. The spin−orbit splitting contributes to the duplicate peaks shown in the Nb 3d, Mo 3d, and W4f states. For simplification, the lower binding energy peaks are marked for indicating the oxidation states of transition metals. All gray lines correspond to the Shirley-type fitting background.

upon cycling. Calculated from CV curves, the first cycle capacity for $W_3Nb_2O_{14}$ is around 136 mAh g^{-1}, in good agreement with the GV experiment at C/10 and close to the theoretical capacity of 139 mAh g^{-1}. Over the first four cycles, there is effectively no change in capacity. The capacity of 220 mAh g^{-1} for the first four cycles of $Mo_3Nb_2O_{14}$ is also consistent with the GV measurements and exceeds the theoretical capacity of 192 mAh g^{-1} based on the 5-electron redox process, which indicates greater than 1 electron per transition-metal ion.

In a second series of CV experiments, the kinetic properties of the two bronzes were characterized by determining the sweep rate dependence. In a CV experiment, the current response i upon varying the sweep rate ν can be determined by a power-law relationship[44]

$$i(\nu) = a\nu^b$$

where a is a constant and b is the power-law exponent. If the b-value is equal to or close to 0.5, charge storage kinetics are considered to be diffusion-controlled processes restricted by semi-infinite diffusion. If the b-value is equal to or close to 1, this corresponds to a capacitor-like process where the current response is dominated by surface adsorption or rapid surface-controlled redox reactions. In the case of $W_3Nb_2O_{14}$, the peak at 2.1 V shows a b-value of 0.85 while the peak at 1.7 V has a b-value of 0.95. Moreover, the box-like shape is maintained at all sweep rates. These features, in combination with the linear dQ/dV values from the GV measurements, indicate that

surface-controlled redox reactions dominate the charge storage kinetics of $W_3Nb_2O_{14}$.

The kinetics for $Mo_3Nb_2O_{14}$ exhibits very different behavior. The irreversible peak initially present in $Mo_3Nb_2O_{14}$ is no longer evident at higher scan rates, and the box-like CV curve changes permanently into broad redox peaks when the scan rate is above 0.5 mV s^{-1}. Because of the irreversible change in the CV curve with increasing scan rate, b-value analysis for $Mo_3Nb_2O_{14}$ could not accurately represent the actual electrode kinetics. Thus, a complementary kinetics analysis method developed by Trasatti et al. was used,[45] as described in the Supporting Information and shown in Figure S7(a−c). Prior to the CV curve change in $Mo_3Nb_2O_{14}$, the kinetics are consistent with a surface-controlled faradaic process, while after the shape change in CV, charge storage is largely diffusion-controlled. Another parameter which is sensitive to the change in CV shape is the overpotential. Using GITT (described in Supporting Information), the overpotential value for $W_3Nb_2O_{14}$ is similar to that of $Mo_3Nb_2O_{14}$ before the shape change, as shown in Figure S9. The significant increase in overpotential after the CV shape change indicates very different electrode kinetics for $Mo_3Nb_2O_{14}$.

Oxidation and Reduction of the Transition Metals. An *ex situ* XPS study was used to identify the oxidation states of the transition metals as well as to provide insight regarding the mechanism associated with the irreversible CV peak in $Mo_3Nb_2O_{14}$. High-resolution scans of Mo and Nb 3d peaks were collected for the as-prepared (pristine) powder, for the

Table 1. Summary of the Oxidation States of Transition Metals and the Calculated Amount of Li Insertion from Figure 5

$Mo_3Nb_2O_{14}$									
E vs Li/Li$^+$	% Mo^{6+}	% Mo^{5+}	% Mo^{4+}	average	% Nb^{5+}	% Nb^{4+}	% Nb^{3+}	average	total Li insertion	Exp Li inserted
OCV	100	0	0	6$^+$	100	0	0	5$^+$	0	0
2.4 V	58.5	28.0	13.5	5.45$^+$	86.2	13.8	0.0	4.86$^+$	1.93	1.88
2.1 V	44.2	30.6	25.2	5.19$^+$	54.7	45.3	0.0	4.55$^+$	3.34	3.23
1.8 V	28.1	37.4	34.5	4.94$^+$	44.0	36.0	20.0	4.24$^+$	4.71	4.69
1.5 V	15.2	37.7	47.1	4.68$^+$	30.3	43.9	25.8	4.04$^+$	5.87	5.89
3.0 V	90.3	9.7	0.0	5.90$^+$	100.0	0.0	0.0	5.00$^+$		

$W_3Nb_2O_{14}$									
E vs Li/Li+	% W^{6+}	% W^{5+}	% W^{4+}	average	% Nb^{5+}	% Nb^{4+}	% Nb^{3+}	Average	total Li insertion	exp Li inserted
OCV	100	0	0	6$^+$	100	0	0	5$^+$	0	0
2.1 V	61.6	26.4	12.0	5.50$^+$	89.8	10.2	0.0	4.90$^+$	1.72	1.47
1.8 V	46.2	32.3	21.5	5.25$^+$	72.5	27.5	0.0	4.72$^+$	2.81	2.52
1.5 V	31.0	39.5	29.5	5.01$^+$	46.3	38.5	15.2	4.31$^+$	4.34	4.04
1.2 V	20.5	47.0	32.5	4.88$^+$	23.0	61.7	15.3	4.08$^+$	5.21	5.37
3.0 V	100	0	0	6$^+$	100	0	0	5$^+$		

first cycle of $Mo_3Nb_2O_{14}$ discharged between 2.8 and 1.5 V and the subsequent charge back to 3.0 V [Figures 5(a−c)]. The XPS of the pristine $Mo_3Nb_2O_{14}$ sample shows that both transition metals are in their highest oxidation states. After the first discharge to 1.5 V, both Mo and Nb go to lower oxidation states, which suggests that each transition metal contributes to the redox reaction during the lithiation process. The quantitative analysis and evolution of oxidation states for the transition metals as a function of potential are summarized in Table 1. The method used in the computation is described in the Supporting Information, and the fitting parameters are listed in Tables S3 and S4. The changes in the oxidation state of the transition metals in both $Mo_3Nb_2O_{14}$ and $W_3Nb_2O_{14}$ as a function of potential during the first discharge cycle are shown in Figure S11. The average oxidation state of Mo is 4.68$^+$, and that of Nb is 4.04$^+$ after the first lithiation, which accounts for a total of 5.87 lithium ions inserted or 225.5 mAh g^{-1}. The capacity calculated from XPS is in good agreement with the measured capacity obtained from the GV at C/10 and the CV at 0.1 mV s^{-1}.

The XPS data collected at 3.0 V after the first cycle indicate that all Nb returns to the 5$^+$ state but that the average Mo oxidation state is 5.9$^+$ as compared to 6$^+$. This result suggests that the irreversible peak in the CV of $Mo_3Nb_2O_{14}$ at 2.4 V (Figure 4a) arises from an incomplete redox reaction with Mo. We examined this hypothesis by characterizing XPS spectra for the Li 1s peak at 3.0 V when all lithium should be removed from the lattice. As shown in Figure S12, residual Li is detected at 3.0 V after the first GV cycle. This peak has an even greater intensity once the CV curve change has occurred in $Mo_3Nb_2O_{14}$. In contrast, both W and Nb in $W_3Nb_2O_{14}$ exhibit good reversibility as they return to their highest oxidation states after charging back to 3 V [Figure 5(d−f)]. In Figure S11, upon lithiation to 1.2 V, the average oxidation state of W is 4.88$^+$, and that of Nb is 4.08$^+$, similar to the values obtained for Mo and Nb in $Mo_3Nb_2O_{14}$, which confirms that both tungsten and niobium undergo redox reactions contributing to charge storage. It is interesting to note that the average oxidation state of Nb is similar in $W_3Nb_2O_{14}$ and $Mo_3Nb_2O_{14}$, and the average oxidation state of W in $W_3Nb_2O_{14}$ is higher than that of Mo in $Mo_3Nb_2O_{14}$, even though the cutoff voltage for $W_3Nb_2O_{14}$ was lower (1.2 V vs 1.5 V). This difference in

oxidation state explains why the capacity is higher in $Mo_3Nb_2O_{14}$ at lower charge/discharge rates.

Structural Changes upon Oxidation and Reduction. Both electrochemical and XPS experiments indicated that irreversible reactions occurred during the initial cycle of $Mo_3Nb_2O_{14}$. To establish the nature of the structural changes associated with the irreversible reactions, *in situ* XRD experiments were conducted at a C/10 rate for the first cycle of both $Mo_3Nb_2O_{14}$ and $W_3Nb_2O_{14}$ as illustrated in Figure 6a and Figure 6c, respectively. The Le Bail XRD refinement for the lattice parameter changes in $Mo_3Nb_2O_{14}$ and $W_3Nb_2O_{14}$ during the first cycle are shown in Figure 6e and Figure 6f, respectively. The selected peaks from the (540) and (600) planes of $Mo_3Nb_2O_{14}$ shown in Figure 6b display a small discontinuous shift in the first discharge cycle at 2.4 V (vs Li/Li$^+$). This potential corresponds to the irreversible peak observed in the CV of $Mo_3Nb_2O_{14}$ (Figure 4a). The discontinuity disappears when charging back to 3.0 V. Even though there is a discontinuous shift of the XRD peak, no new peaks are observed, implying that an irreversible structural rearrangement is associated with the irreversibility of the peak exhibited in CV. The entropic potential measurements (described in the Supporting Information) are consistent with the structural rearrangement as shown by nonoverlapped entropic potentials and an abnormal decrease in apparent lithium diffusion coefficient in the first cycle of $Mo_3Nb_2O_{14}$ (Figure S15).

It is important to note that selected XRD peak positions after the first cycle charging to 3.0 V do not move back to the original positions, indicating a change in lattice parameters. Specifically, the interplanar distance of (540) and (600) plane increases, illustrating that the *a-b* plane undergoes an expansion after the first cycle and the distance in the *c* direction decreases since the peak position of (001) plane shifts to the right. To determine whether the accumulation of irreversible redox reactions would bring a continuous change in lattice parameters, *operando* XRD of more cycles of $Mo_3Nb_2O_{14}$ was performed at the C/3 rate shown in Figure S16. The discontinuous peak shift observed in the first discharge cycle of the *in situ* XRD pattern (Figure 6b) also occurs in the *operando* XRD. The selected peak from the (330) plane shows that even though the shift per cycle becomes smaller due to lower capacity at high rate, the peak keeps
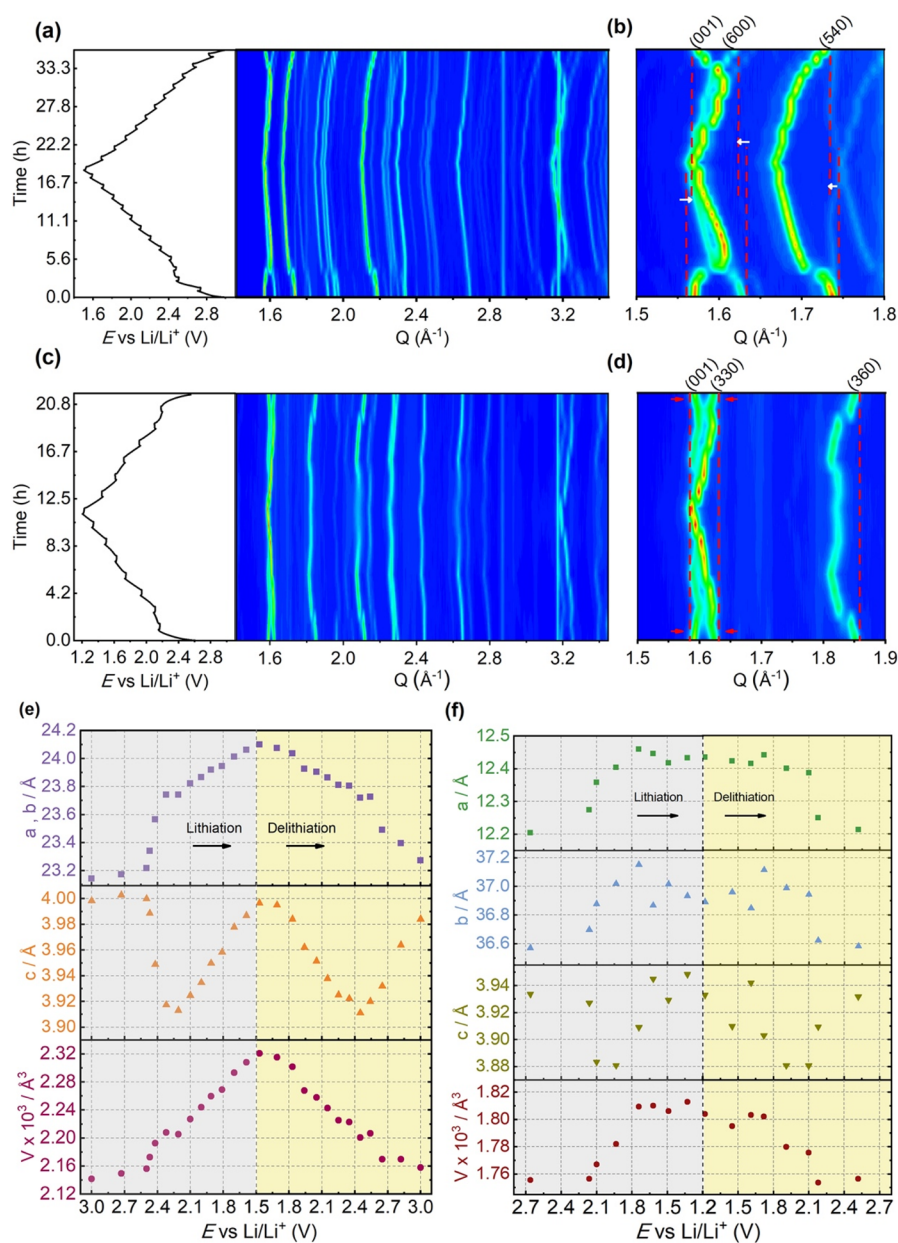
Figure 6. *In situ* XRD patterns of (a) $Mo_3Nb_2O_{14}$ discharged to 1.5 V and charged to 3.0 V at a C/10 rate and (c) $W_3Nb_2O_{14}$ discharged to 1.2 V and charged to 3.0 V at a C/10 rate. Selected Q range in *in situ* XRD pattern of (b) (001), (600), and (540) plane of $Mo_3Nb_2O_{14}$ or (d) (001), (330), and (360) plane of $W_3Nb_2O_{14}$. Resolved lattice parameters and unit cell volume variations during discharging and charging at C/10 rate from Le Bail refinement of (e) $Mo_3Nb_2O_{14}$ or (f) $W_3Nb_2O_{14}$.

shifting in the same direction to a low Q value during cycling, confirming the accumulation of permanent lattice expansions in the *a*-*b* plane. The lattice parameters shown in Figure 6e indicate lattice expansion in both the *a* and *b* directions and shrinkage in the *c* direction after the first cycle. The increase in *a*-*b* direction first followed by the *c* direction is commonly seen in the bronze phase structure.[7,46] Lithium ions preferentially occupy the large channel located in the *a*-*b* plane causing expansion of the *a*-*b* plane before starting to occupy the sites in the *c* direction that lead to an increase in the *c* direction.

In the case of $W_3Nb_2O_{14}$, a reversible structural rearrangement is suggested by *in situ* XRD for the tiny discontinuity shown at 2.1 V. The *a* and *b* directions of $W_3Nb_2O_{14}$ increase first and then decrease when the *c* direction starts to increase, which compensates for the entire volume expansion and leads

to only 3% volume expansion in the fully lithiated state. This value is significantly smaller than that of $Mo_3Nb_2O_{14}$, which is calculated to be 8%. Unlike $Mo_3Nb_2O_{14}$, all XRD peaks in $W_3Nb_2O_{14}$ return to their original positions, as shown by the (001), (330), and (360) planes shown in Figure 6d as examples. A similar *operando* XRD pattern was collected at a C/3 rate for more cycles in $W_3Nb_2O_{14}$. As shown by the peak from the (430) plane (Figure S17), the nearly identical peak positions after each cycle clearly indicate the better structural reversibility of $W_3Nb_2O_{14}$ over $Mo_3Nb_2O_{14}$. The smaller change in lattice parameters in $W_3Nb_2O_{14}$ is identified from both the lattice parameters and the magnitude of the peak shift in the *in situ* XRD pattern. The structural reversibility was also verified by an entropic potential measurement (Figure S15) that exhibits an overlapped entropic potential in the first two

cycles, which indicates the stability of the electrode materials. The smaller volume expansion and better structural reversibility revealed from *in situ* and *operando* XRD explain the superior long-term cycling stability, Coulombic efficiency, and electrochemical reversibility of $W_3Nb_2O_{14}$ compared to $Mo_3Nb_2O_{14}$.

4. CONCLUSIONS

Bronze phase materials with tunnel-like structures offer a promising direction for fast charging battery electrodes, particularly for systems with two transition metals. The current studies focused on determining the role of the transition metal in two different bronze phase compositions having the same stoichiometry: $W_3Nb_2O_{14}$ and $Mo_3Nb_2O_{14}$. While the Nb in both phases exhibited similar redox properties, the Mo provides much greater redox than W, achieving >1 electron per transition metal at rates below C/2. However, the Mo does not return to the 6^+ state on oxidation, leading to lithium accumulation, permanent lattice expansion in the *a-b* plane, and poor capacity at high rates. The $W_3Nb_2O_{14}$ material exhibits much better structural reversibility on cycling as the XRD peaks return to their original positions; the open bronze structure is retained, and the capacity of $W_3Nb_2O_{14}$ exceeds that of $Mo_3Nb_2O_{14}$ at rates above 10C. Thus, while molybdenum could offer an increase in capacity in the battery electrode, it might not be a good choice as part of a building block that retains an open framework on cycling. These results underscore the important role of the transition metal in the bronze phase in terms of structure stability and electrode kinetics and provide insight into the design of bronze phases for high energy and high power density electrodes.

■ ASSOCIATED CONTENT

ⓢ Supporting Information

The Supporting Information is available free of charge at https://pubs.acs.org/doi/10.1021/acs.chemmater.3c01860.

> CV potential window opening experiment of $W_3Nb_2O_{14}$ and $Mo_3Nb_2O_{14}$. SEM/EDX images and statistical results for $Mo_3Nb_2O_{14}$ and $W_3Nb_2O_{14}$. High resolution TEM, EDX elemental mapping and preferential transition metal occupancy of $W_3Nb_2O_{14}$. Trasatti method measurement for electrode kinetics of $Mo_3Nb_2O_{14}$ and $W_3Nb_2O_{14}$. GITT and overpotential measurements of $Mo_3Nb_2O_{14}$ and $W_3Nb_2O_{14}$. XPS of $Mo_3Nb_2O_{14}$ with gradually increasing residual Li during cycling. XPS fitting parameters. Oxidation state of transition metal change in the first discharge cycle for both $W_3Nb_2O_{14}$ and $Mo_3Nb_2O_{14}$. Entropic potential measurements of $Mo_3Nb_2O_{14}$ and $W_3Nb_2O_{14}$. *Operando* XRD patterns for multiple cycles of $Mo_3Nb_2O_{14}$ and $W_3Nb_2O_{14}$ at C/3 rate (PDF)

■ AUTHOR INFORMATION

Corresponding Author

Bruce Dunn − *Department of Materials Science and Engineering, University of California, Los Angeles 90095 California, United States;* ⓞ orcid.org/0000-0001-5669-4740; Email: bdunn@ucla.edu

Authors

Yunkai Luo − *Department of Materials Science and Engineering, University of California, Los Angeles 90095 California, United States;* ⓞ orcid.org/0000-0002-1949-5395

Etienne Le Calvez − *Institut des Matériaux de Nantes Jean Rouxel, IMN, Nantes F-44000, France; Réseau sur le Stockage Electrochimique de l'Energie (RS2E), CNRS FR 3459, Amiens Cedex 80039, France*

Yucheng Zhou − *Department of Mechanical and Aerospace Engineering, University of California, Los Angeles 90095 California, United States*

Éric Gautron − *Institut des Matériaux de Nantes Jean Rouxel, IMN, Nantes F-44000, France*

Éric Quarez − *Institut des Matériaux de Nantes Jean Rouxel, IMN, Nantes F-44000, France;* ⓞ orcid.org/0000-0001-7887-892X

Molleigh Preefer − *Stanford Synchrotron Radiation Lightsource, SLAC National Accelerator Laboratory, Menlo Park 94025 California, United States;* ⓞ orcid.org/0000-0002-3699-8613

Olivier Crosnier − *Institut des Matériaux de Nantes Jean Rouxel, IMN, Nantes F-44000, France; Réseau sur le Stockage Electrochimique de l'Energie (RS2E), CNRS FR 3459, Amiens Cedex 80039, France*

Johanna Nelson Weker − *Stanford Synchrotron Radiation Lightsource, SLAC National Accelerator Laboratory, Menlo Park 94025 California, United States;* ⓞ orcid.org/0000-0001-6856-3203

Laurent Pilon − *Department of Mechanical and Aerospace Engineering, University of California, Los Angeles 90095 California, United States;* ⓞ orcid.org/0000-0001-9459-8207

Thierry Brousse − *Institut des Matériaux de Nantes Jean Rouxel, IMN, Nantes F-44000, France; Réseau sur le Stockage Electrochimique de l'Energie (RS2E), CNRS FR 3459, Amiens Cedex 80039, France;* ⓞ orcid.org/0000-0002-1715-0377

Complete contact information is available at:
https://pubs.acs.org/10.1021/acs.chemmater.3c01860

Notes

The authors declare no competing financial interest.

■ ACKNOWLEDGMENTS

■ REFERENCES

(1) U. S. Energy Information Administration *Monthly Energy Review*, April 2021.

(2) Sanguesa, J. A.; Torres-Sanz, V.; Garrido, P.; Martinez, F. J.; Marquez-Barja, J. M. A Review on Electric Vehicles: Technologies and Challenges. *Smart Cities* **2021**, *4*, 372−404.

(3) Shen, C.; Hu, G.; Cheong, L. Z.; Huang, S.; Zhang, J. G.; Wang, D. Direct Observation of the Growth of Lithium Dendrites on Graphite Anodes by Operando EC-AFM. *Small Methods* **2018**, *2*, 1700298.

(4) Yi, T.-F.; Yang, S.-Y.; Xie, Y. Recent advances of $Li_4Ti_5O_{12}$ as a promising next generation anode material for high power lithium-ion batteries. *J. Mater. Chem. A* **2015**, *3*, 5750−5777.

(5) Han, J.-T.; Huang, Y.-H.; Goodenough, J. B. New Anode Framework for Rechargeable Lithium Batteries. *Chem. Mater.* **2011**, *23*, 2027−2029.

(6) Preefer, M. B.; Saber, M.; Wei, Q.; Bashian, N. H.; Bocarsly, J. D.; Zhang, W.; Lee, G.; Milam-Guerrero, J.; Howard, E. S.; Vincent, R. C.; et al. Multielectron Redox and Insulator-to-Metal Transition upon Lithium Insertion in the Fast-Charging, Wadsley-Roth Phase PNb_9O_{25}. *Chem. Mater.* **2020**, *32*, 4553−4563.

(7) Griffith, K. J.; Wiaderek, K. M.; Cibin, G.; Marbella, L. E.; Grey, C. P. Niobium tungsten oxides for high-rate lithium-ion energy storage. *Nature* **2018**, *559*, 556−563.

(8) Kong, F.; Liang, X.; Yi, L.; Fang, X.; Yin, Z.; Wang, Y.; Zhang, R.; Liu, L.; Chen, Q.; Li, M.; et al. Multi-electron reactions for the synthesis of a vanadium-based amorphous material as lithium-ion battery cathode with high specific capacity. *Energy* **2021**, *219*, 119513.

(9) Xu, X.; Xiong, F.; Meng, J.; An, Q.; Mai, L. Multi-electron reactions of vanadium-based nanomaterials for high-capacity lithium batteries: challenges and opportunities. *Mater. Today Nano* **2020**, *10*, 100073.

(10) Vincent, R. C.; Luo, Y.; Andrews, J. L.; Zohar, A.; Zhou, Y.; Yan, Q.; Mozur, E. M.; Preefer, M. B.; Weker, J. N.; Cheetham, A. K.; et al. High-Rate Lithium Cycling and Structure Evolution in Mo_4O_{11}. *Chem. Mater.* **2022**, *34*, 4122−4133.

(11) Vincent, R. C.; Cheetham, A. K.; Seshadri, R. Structure and lithium insertion in oxides of molybdenum. *APL Mater.* **2023**, *11*, No. 010902.

(12) Kim, H.-S.; Cook, J. B.; Lin, H.; Ko, J. S.; Tolbert, S. H.; Ozolins, V.; Dunn, B. Oxygen vacancies enhance pseudocapacitive charge storage properties of $MoO_{3−x}$. *Nat. Mater.* **2017**, *16*, 454−460.

(13) Wyckoff, K. E.; Robertson, D. D.; Preefer, M. B.; Teicher, S. M. L.; Bienz, J.; Kautzsch, L.; Mates, T. E.; Cooley, J. A.; Tolbert, S. H.; Seshadri, R. High-Capacity Li^+ Storage through Multielectron Redox in the Fast-Charging Wadsley−Roth Phase $(W_{0.2}V_{0.8})_3O_7$. *Chem. Mater.* **2020**, *32*, 9415−9424.

(14) Chen, Z.; Ye, K.; Li, M.; Zhao, S.; Luo, J.; Wu, B. Lithiation mechanism of $W_{18}O_{49}$ anode material for lithium-ion batteries: Experiment and first-principles calculations. *J. Electroanal. Chem.* **2021**, *880*, 114885.

(15) Wöhler, F. Über das wolfram. *Ann. Phys.* **1824**, *78*, 345−358.

(16) Dickens, P. G.; Whittingham, M. S. The tungsten bronzes and related compounds. *Q. Rev., Chem. Soc.* **1968**, *22*, 30−44.

(17) Ribnick, A. S.; Post, B.; Banks, E. Phase Transitions in Sodium Tungsten Bronzes In Nonstoichiometric Compounds. *Am. Chem. Soc.* **1963**, *39*, 246−253.

(18) Espinosa-Angeles, J. C.; Quarez, E.; Mvele Eyé'a, L.-B.; Douard, C.; Iadecola, A.; Shao, H.; Taberna, P.-L.; Simon, P.; Crosnier, O.; Brousse, T. Charge Storage Mechanism of Li_xWO_3 Hexagonal Tungsten Bronze in Aqueous Electrolytes. *Batteries* **2023**, *9*, 136.

(19) Tong, X.; Wang, J.; Zhang, P.; Lei, P.; Gao, Y.; Ren, R.; Zhang, S.; Zhu, R.; Cai, G. Insight into the structure−activity relationship in electrochromism of WO_3 with rational internal cavities for broadband tunable smart windows. *Chem. Eng. J.* **2023**, *470*, 144130.

(20) Cheng, K. H.; Stanley Whittingham, M. Lithium incorporation in tungsten oxides. *Solid State Ionics* **1980**, *1*, 151−161.

(21) de la Cruz, A. M.; García-Alvarado, F.; Morán, E.; Alario-Franco, M. A.; Torres-Martínez, L. M. Lithium in $W_{18}O_{49}$: synthesis and characterization of novel phases. *J. Mater. Chem.* **1995**, *5*, 513−516.

(22) Shen, C.; Jiang, S.; Ding, C.; Xue, W.; Xie, K. Lithium-ion diffusion path of tetragonal tungsten bronze (TTB) phase $Nb_{18}W_{16}O_{93}$. *Trans. Nonferrous Met. Soc. China* **2022**, *32*, 3679−3686.

(23) Saritha, D. Electrochemical analysis of tungsten bronze-type phases, $W_9Nb_8O_{47}$ and $W_7Nb_4O_{31}$, synthesised by sol-gel method. *Mater. Sci. Eng., B* **2018**, *228*, 218−223.

(24) Yan, L.; Cheng, X.; Yu, H.; Zhu, H.; Liu, T.; Zheng, R.; Zhang, R.; Shui, M.; Shu, J. Ultrathin $W_9Nb_8O_{47}$ nanofibers modified with thermal NH_3 for superior electrochemical energy storage. *Energy Storage Mater.* **2018**, *14*, 159−168.

(25) Yao, W.; Zhu, H.; Wang, M.; Li, P.; Liu, P.; Zou, P.; Nie, A.; Wang, G.; Kang, F.; Yang, C. Structural Insights into the Lithium Ion Storage Behaviors of Niobium Tungsten Double Oxides. *Chem. Mater.* **2022**, *34*, 388−398.

(26) Kaveevivitchai, W.; Jacobson, A. J. High Capacity Microporous Molybdenum−Vanadium Oxide Electrodes for Rechargeable Lithium Batteries. *Chem. Mater.* **2013**, *25*, 2708−2715.

(27) Rödel, E.; Timpe, O.; Trunschke, A.; Zenkovets, G. A.; Kryukova, G. N.; Schlögl, R.; Ressler, T. Structure stabilizing effect of tungsten in mixed molybdenum oxides with Mo_5O_{14}-type structure. *Catal. Today* **2007**, *126*, 112−118.

(28) Ekström, T. Formation of ternary phases of Mo_5O_{14} and $Mo_{17}O_{47}$ structure in the molybdenum-wolfram-oxygen system. *Mater. Res. Bull.* **1972**, *7*, 19−26.

(29) Hashem, A. M.; Abdel-Ghany, A. E.; El-Tawil, R. S.; Indris, S.; Ehrenberg, H.; Mauger, A.; Julien, C. M. Amorphous Mo_5O_{14}-Type/ Carbon Nanocomposite with Enhanced Electrochemical Capability for Lithium-Ion Batteries. *Nanomaterials* **2020**, *10*, 2079−4991.

(30) Ette, P. M.; Babu, D. B.; Roy, M. L.; Ramesha, K. $Mo_3Nb_2O_{14}$: A high-rate intercalation electrode material for Li-ion batteries with liquid and garnet based hybrid solid electrolytes. *J. Power Sources* **2019**, *436*, 226850.

(31) Fang, X.; Rong, C.; Zhou, L.; Yin, C.; He, L.; Cui, H.; Lu, F.; Kuang, X. Enhanced Lithium Storage in Micrometer-Scale Tungsten Bronze $Mo_3Nb_2O_{14}$ by Molybdenum Reduction and Oxygen Deficiency. *Adv. Mater. Interfaces* **2021**, *8*, 2101016.

(32) Petříček, V.; Dušek, M.; Palatinus, L. Crystallographic Computing System JANA2006: General Features. *Zeitschrift für Kristallographie - Crystalline Materials* **2014**, *229*, 345−352, DOI: 10.1515/zkri-2014-1737.

(33) Leriche, J. B.; Hamelet, S.; Shu, J.; Morcrette, M.; Masquelier, C.; Ouvrard, G.; Zerrouki, M.; Soudan, P.; Belin, S.; Elkaïm, E.; Baudelet, F. An Electrochemical Cell for Operando Study of Lithium Batteries Using Synchrotron Radiation. *J. Electrochem. Soc.* **2010**, *157*, A606.

(34) Baek, S. W.; Preefer, M. B.; Saber, M.; Zhai, K.; Frajnkovič, M.; Zhou, Y.; Dunn, B. S.; Van der Ven, A.; Seshadri, R.; Pilon, L. Potentiometric entropy and operando calorimetric measurements reveal fast charging mechanisms in PNb_9O_{25}. *J. Power Sources* **2022**, *520*, 230776.

(35) Baek, S. W.; Wyckoff, K. E.; Butts, D. M.; Bienz, J.; Likitchatchawankun, A.; Preefer, M. B.; Frajnkovič, M.; Dunn, B. S.; Seshadri, R.; Pilon, L. Operando calorimetry informs the origin of rapid rate performance in microwave-prepared $TiNb_2O_7$ electrodes. *J. Power Sources* **2021**, *490*, 229537.

(36) Zhou, Y.; Le Calvez, E.; Baek, S. W.; Frajnkovič, M.; Douard, C.; Gautron, E.; Crosnier, O.; Brousse, T.; Pilon, L. Effect of particle size on thermodynamics and lithium ion transport in electrodes made of $Ti_2Nb_2O_9$ microparticles or nanoparticles. *Energy Storage Mater.* **2022**, *52*, 371−385.

(37) Bouillaud, Y. Mise en évidence et étude cristallographique d'une solution solide entre les composés $NaNb_3O_8$ et $Nb_2W_3O_{14}$. *Bull. Soc. fr. minéral. cristallogr.* **1968**, *91*, 289−291.

(38) Vakarin, S. V.; Baraboshkin, A. N.; Kaliev, K. A.; Zyrianov, V. G. Crystal growth of tungsten bronzes with a hexagonal structure. *J. Cryst. Growth* **1995**, *151*, 121−126.

(39) Ette, P. M.; Babu, D. B.; Roy, M. L.; Ramesha, K. $Mo_3Nb_2O_{14}$: A high-rate intercalation electrode material for Li-ion batteries with liquid and garnet based hybrid solid electrolytes. *J. Power Sources* **2019**, *436*, 226850.

(40) Barthel, J. Dr. Probe: A software for high-resolution STEM image simulation. *Ultramicroscopy* **2018**, *193*, 1−11.

(41) Wörle, M.; Krumeich, F. On the structural complexity of tetragonal tungsten bronze type niobium tungsten oxides. *Z. Anorg. Allg. Chem.* **2021**, *647*, 98−106.

(42) Krumeich, F. The Complex Crystal Chemistry of Niobium Tungsten Oxides. *Chem. Mater.* **2022**, *34*, 911−934.

(43) Choi, C.; Ashby, D. S.; Butts, D. M.; DeBlock, R. H.; Wei, Q.; Lau, J.; Dunn, B. Achieving high energy density and high power density with pseudocapacitive materials. *Nat. Rev. Mater.* **2020**, *5*, 5−19.

(44) Augustyn, V.; Come, J.; Lowe, M. A.; Kim, J. W.; Taberna, P.-L.; Tolbert, S. H.; Abruña, H. D.; Simon, P.; Dunn, B. High-rate electrochemical energy storage through Li^+ intercalation pseudocapacitance. *Nat. Mater.* **2013**, *12*, 518−522.

(45) Ardizzone, S.; Fregonara, G.; Trasatti, S. Inner" and "outer" active surface of RuO_2 electrodes. *Electrochim. Acta* **1990**, *35*, 263−267.

(46) Kim, Y.; Jacquet, Q.; Griffith, K. J.; Lee, J.; Dey, S.; Rinkel, B. L. D.; Grey, C. P. High Rate Lithium Ion Battery with Niobium Tungsten Oxide Anode. *J. Electrochem. Soc.* **2021**, *168*, No. 010525.